Article:
Pradhan, S., Solomon, R., Gangotra, A. et al. (5 more authors) (2021) Depletion of HP1α alters the mechanical properties of MCF7 nuclei. Biophysical Journal, 120 (13). pp. 2631-2643. ISSN: 0006-3495

https://doi.org/10.1016/j.bpj.2021.05.017

Manuscript submitted to **Biophysical** *Journal*
Article

Depletion of HP1α alters the mechanical properties of MCF7 nuclei

SP[1,2], RS[1], AG[2,3], GEY[4,5], GRW[2,3], CPW[1,2], TKH[*1], and MAKW[*1,2]

[*]Correspondence:

ABSTRACT Within the nucleus of the eukaryotic cell, DNA is partitioned into domains of transcriptionally active euchromatin and highly condensed transcriptionally-silent heterochromatin. Heterochromatin-protein 1α (HP1α) is an architectural protein that establishes and maintains heterochromatin, thus ensuring genome fidelity and nuclear integrity. During tumour cell invasion, the malleability of the nuclear periphery increases so that the cell can more easily migrate through spaces in the surrounding tissue. The onset of this invasion correlates with the loss of HP1α in many solid tumours. For example, poorly invasive MCF7 breast cancer cells become more invasive following a knock-down of HP1α. Herein, Atomic Force Microscopy (AFM), Optical Tweezers (OT) and Micropipette Aspiration (MA) were each used to characterize the mechanical properties of nuclei extracted from HP1α knock-down or matched control MCF7 cells. When using AFM or OT to probe the nuclear periphery, the nuclei extracted from MCF7 HP1α knock-down cells were found to have apparent Young's moduli that were significantly lower than the control MCF7 nuclei, supporting the hypothesis that modification of these mechanical properties via this mechanism is linked to invasiveness. Results from the MA experiments were determined by deformation of the whole nuclei as opposed to the localized deformation probed by AFM and OT. The observed differences in chromatin patterning and lamina morphology between the MCF7 control and HP1α knock-down nuclei correlated with our quantitative mechanical measurements. Our findings suggest that loss of HP1α causes a disruption to the nuclear periphery making the nuclei, and thereby the cells, more malleable, thus increasing their invasive potential, while maintaining nuclear integrity.

INTRODUCTION

The eukaryotic nucleus is defined by the nuclear envelope which is composed of the outer nuclear membrane and inner nuclear membrane. Lining the inner nuclear membrane is the lamina, a proteinaceous layer comprised of separate but interconnected intermediate filament networks of A-type lamin (A and C) and B-type lamin (B1 and B2) proteins (1–4). This barrier houses the genome, where DNA is wrapped around histone proteins to form chromatin fibres that undergo further levels of folding to create domains of highly condensed transcriptionally-silent heterochromatin and domains of less compact transcriptionally-active euchromatin (5, 6). This compartmentalisation of the genome determines patterns of gene expression and thus cell identity. Heterochromatin protein 1α (HP1α) is an architectural protein that forms and maintains compact domains of heterochromatin (7, 8), and also contributes to the sequestration of heterochromatin at the nuclear periphery through its interactions with proteins embedded in the nuclear membrane and lamina (7, 9–11). This network of interactions between the nuclear envelope, the underlying lamina and the adjacent heterochromatin ensure both nuclear and genomic integrity (12–15).

As the largest cellular organelle, the nucleus is also a major physical entity, where the nuclear lamina and heterochromatin are key mechanical components (16). It is the A-type lamin network that provides stiffness to the nucleus, while B-type lamins have been shown to contribute to nuclear elasticity (17, 18). Depletion of lamin A results in a loss of nuclear rigidity (19, 20), a reduction of chromatin-lamina attachments, and the loss of heterochromatin (21, 22). In differentiated cells, it is found that the retention of heterochromatin at the nuclear periphery renders the nucleus less malleable whereas a more diffuse pattern of stem cell-like heterochromatin increases nuclear plasticity (23, 24). Micromanipulation and atomic force microscope studies have reinforced the contribution heterochromatin makes to the mechanical properties of the nucleus. These studies showed the rigidity of the nucleus was influenced by the compaction state of chromatin, as nuclei are weakened by reducing the overall level of heterochromatin or by increasing the level of euchromatin, which can lead to nuclear blebbing and rupture (19, 25).

Nuclear deformation is the rate limiting step for cell migration through small constrictions in three-dimensional environments of the tissue (26, 27). The modulation of HP1α expression in malignant breast cell lines indicates that HP1α can suppress the invasive potential of cells (28). In the poorly invasive breast cell MCF7 line, constitutive knock-down (KD) of HP1α has been shown to increase the ability of cells to move through a three-dimensional extracellular matrix, while introduction of HP1α into highly invasive MDA-MB-231 breast cancer cells, with low endogenous levels of HP1α, suppresses their invasive

potential *in vitro* (28, 29). These findings are supported by the correlation of reduced HP1α expression with the onset of malignant cell invasion in many solid tumours, including those of the thyroid and breast (29–31). Given the role of HP1α in heterochromatin organisation, this raises the possibility that reduction of HP1α aids malignant cell invasion, not only by disrupting gene silencing but also by altering the mechanical properties of the nucleus.

Various techniques (32) have been used to characterize the mechanical properties of nuclei of different cell types, including AFM indentation (23, 33, 34) and micropipette aspiration (MA) (23, 24, 35–37). The elastic modulus measured using these techniques ranges from 1-15 kPa. In this study, we have used a combination of AFM, optical tweezers (OT) and MA techniques to characterize the mechanical properties of nuclei isolated from MCF7 control and HP1α KD cells. Longitudinal indentation (into the top of the surface-bound nucleus) was complemented by a lateral indentation (into the side) of MCF7 nuclei. Lateral indentation has the advantage of avoiding the passage of the laser through the nuclei that might lead to damage, heating and bead tracking fluctuations. We demonstrate using AFM and OT techniques that HP1α KD decreases the elasticity of the nuclear periphery by an order of magnitude as compared to MCF7 control nuclei, thereby promoting enhanced malleability. This decrease in elasticity is associated with peripheral heterochromatin and nuclear lamina that is more disorganised in HP1α KD cells. In contrast the mechanical properties assessed by MA showed little difference in the deformation of the whole nuclei between HP1α KD and control nuclei, implying that reduced HP1α expression does not contribute to a decrease in the overall integrity of the nucleus. Finally, we highlight the benefit of using an array of complementary techniques to probe nuclear mechanics.

MATERIALS AND METHODS

Creation and maintenance of the HP1α knock-down cell line

MCF7 (RRID:CVCL_0031) cells (ATCC) with constitutive KD of HP1α were created using Qiagen SureSilencing shRNA plasmids. Briefly, MCF7 cells were transfected with linearized scrambled or HP1α KD shRNA (shRNA 1-4) plasmids using X-tremeGENE 9 DNA Transfection Reagent (Roche). Transformed cells were selected with 200 μg/mL hygromycin B to obtain a polyclonal population of cells to minimize insertional variation. After determining the level of HP1α KD compared to both MCF7 cells and the scrambled shRNA MCF7 control line, the MCF7 HP1α KD line established with shRNA4 (HP1α KD) was used for this study along with the scrambled shRNA MCF7 control line. The MCF7 HP1α KD and matched control line were maintained in DMEM (Gibco) supplemented with 35 μg/mL hygromycin B (Gibco), 10 μg/mL insulin (Sigma-Aldrich), 1% penicillin/streptomycin (Gibco) and 10% fetal bovine serum (FBS; Gibco) at 37°C with 5% CO_2 in a humidified atmosphere.

Isolation of nuclei for biophysical analyses

Asynchronously growing MCF7 cells were harvested at confluence, washed twice with PBS then resuspended in ice cold nuclei extraction buffer (320 mM sucrose, 10 mM HEPES, 5mM $MgCl_2$, 1% Triton X-100, pH 7.4) at a concentration of 1 x 10^6 cells/mL, and vortexed gently for 10 s. The cells were incubated on ice for 15 min, vortexed briefly every 5 min, then centrifuged at 2000 x g for 5 min at 4 °C. The nuclear pellet was resuspended in nuclear wash buffer (320 mM sucrose, 10 mM HEPES, 5 mM $MgCl_2$, pH 7.4), and the nuclei then processed further as required.

Antibodies

The primary antibodies used for this study were HP1α (2616, Cell Signaling Technology), Lamin A/C (ab108595, Abcam), Lamin B2 (ab151735, Abcam), Histone H3K9me2 (ab1220, Abcam), and Histone H3K9me3 (ab8898, Abcam). Secondary antibodies were anti-mouse Alexa 555 (ab150114, Abcam), anti-rabbit Alexa 647 (ab150079, Abcam), HRP-linked anti-mouse (NA931, GE Healthcare) and HRP-linked anti-rabbit (NA934, GE Healthcare).

Immunofluorescence

Asynchronously growing cells adhered to lysine-coated coverslips were washed twice with Phosphate Buffered Saline (PBS) containing $MgCl_2$ and $CaCl_2$, fixed in 4% paraformaldehyde/PBS for 15 min at room temperature (RT) and then washed with PBS. Cells were permeabilized (0.5% Triton X-100, PBS) for 5 min at RT, washed again with PBS, before incubation in blocking buffer (PBS, 5% bovine serum albumin, 0.5% Tween-20) for 30 min at RT. The appropriate primary antibodies (diluted in blocking buffer) were then added to the cells for 16 h at 4°C. After washing (0.1% Triton X-100, PBS), cells were incubated with the appropriate Alexa fluorophore conjugated secondary antibody, washed again and stained with DAPI, before imaging on a Leica SP5 DM6000B Scanning Confocal Microscope using an oil-immersion 63x objective lens (NA 1.4). Laser excitation wavelength, and collection ranges appropriate to the fluorophores of each sample were used to detect the emission

spectra of the specific combination of DAPI (ex 405 nm, em 410-530 nm), and the secondary antibody Alexa fluorophores; 555 (ex 555 nm, em 565-600 nm) or 647 (ex 647, em 670- 720 nm). Z-stacks were collected with a 0.35 µm vertical offset, and projected with maximum intensity. All images were digitally processed for presentation with ImageJ (38).

Cell fractionation and immunoblot analyses

Adapted from Kapoor et al ((39)), cells at 90% confluence were harvested, washed in PBS, and resuspended in Buffer A (20 mM Tris-HCl pH 7.5, 75 mM KCl, 30 mM $MgCl_2$, 1 mM DTT, 0.5 mM EDTA, 0.5% NP40, complete EDTA-free protease inhibitor) to a concentration of 0.5 x 10^6 cells/100 µL, and incubated on ice for 10 min with intermittent mixing. An aliquot was removed and retained as the whole cell lysate fraction. The remaining sample was centrifuged at 7000 x g for 10 min at 4 °C, and the supernatant collected as the cytoplasmic fraction. The remaining pellet was resuspended in Buffer A to provide the nuclear fraction. To isolate the nuclear envelope, 20 x10^6 cells were washed in PBS and the Nuclear Envelope Protein Extraction kit (101Bio; P513L) was used as per manufacturer's instructions. Recovery of nuclear envelope proteins was confirmed by 10% SDS PAGE and detected by staining with Coomassie Brilliant Blue R250. For immunoblot analysis, samples were resolved by 10% SDS-PAGE then transferred to nitrocellulose. The blots were processed as previously described by Tretiakova et al. (30) and visualised using an Azure c600 imaging system (Azure Biosystems).

Salt treatment of nuclei

Isolated nuclei were sequentially resuspended in an ice-cold salt extraction buffer (10 mM Tris pH 7.4, 2 mM $MgCl_2$, 0.1 %Triton X-100, 1mM DTT, complete EDTA-free protease inhibitor) supplemented to increasing NaCl concentrations of 50 mM, 150 mM, 250 mM, 500 mM (modified from Dahl et al. (23)). For each extraction step, the resuspended pellet was incubated for 15 min at 4 °C with gentle nutating, and the soluble material was then separated from the insoluble material by centrifugation at 2000 x g for 10 min at 4 °C. The final insoluble pellet was resuspended in 1x Laemmli buffer, and heated to 99 °C for 5 min, along with equal volumes of extracted soluble material. These were resolved by 10% SDS-PAGE before immunoblot analysis.

Scanning electron microscopy (SEM)

Isolated nuclei adhered to lysine-coated coverslips were fixed in Modified Karnovsky's fixative (3% gluteraldehyde (Merck) (v/v), 2% formaldehyde (w/v) in 0.1 M phosphate buffer, pH 7.2) for at least 8 hours. After rinsing three times in 0.1 M phosphate buffer (pH 7.2), the coverslips were dehydrated in a graded series of aqueous ethanol solutions (25%, 50%, 75%, 95%) for 15 minutes each, then in 100 % ethanol for 1 hour. Samples were critical-point dried using liquid CO_2 as the CP fluid and 100 % ethanol as the intermediary (Polaron E3000 series II critical point drying apparatus). Once dried, samples were mounted on an aluminium stub, sputter coated with approximately 100 nm of gold (BAL-TEC SCD 005 sputter coater) and viewed in a FEI Quanta 200 scanning electron microscope at an accelerating voltage of 20 kV.

Transmission electron microscopy (TEM)

Cells were harvested at confluence, and pelleted at 200 x g for 5 minutes. The pellet was resuspended in molten low-melting point agarose and centrifuged at 8000 x g for 1 minute to form a cell pellet suspended in agarose. The cells were fixed in Modified Karnovsky's fixative for at least 8 h, washed three times in 0.1 M phosphate buffer (pH 7.2) for 10 m, followed by post-fixing in 1% Osmium Tetroxide in 0.1 M phosphate buffer for 1 hour. The sample was then washed as above, dehydrated in a series of graded aqueous acetone mixtures (25%, 50%, 75%, 95%, 100%), infiltrated in an equal mixture of resin and acetone overnight, before embedding in 100% epoxy resin (Procure 812, ProSciTech Australia). The resin was replaced another three times for 8 h or overnight before the epoxy resin was cured at 60°C for 48 h. The embedded samples were cut to 100 nm using a diamond knife (Diatome, Switzerland) on a Leica EM UC7 ultra-microtome (Leica Biosystems, Nussloch, Germany). These cuts were then stretched with chloroform vapour and mounted on grids using a Quick Coat G pen (Daido Sangyo, Japan). The grids were stained with saturated uranyl acetate in 50% and lead citrate. Samples were then examined with a FEI Technai G2 Spirit BioTWIN Transmission Electron Microscope (Czech Republic).

AFM setup

AFM measurements were performed using a JPK Nanowizard II (JPK Instruments, Bruker) mounted on an inverted fluorescent optical microscope (LSM 710, Zeiss). Fig. 1(a) shows schematics of the AFM set up to scale, in order to highlight the size of the cantilever relative to the colloidal probe and the cell. The microscope was equipped with a double illumination optical setup, which enables illumination of top and bottom of the sample at the same time. This allows observation of nuclei in a

high contrast mode under top illumination, whilst being able to observe nuclei and colloidal probe hidden under the cantilever from the bottom (40, 41). This enables accurate positioning of the colloidal probe above the centre of the nucleus (Fig. 1(b)). Indentation measurements were performed using PNP-TR-TL 200 μm long cantilevers ($f_0 \sim 17$ kHz) (NanoWorld), with SiO_2 spheres of 2 μm diameter (Polysciences AG) mounted using a 2 component epoxy glue (UHU Schnellfest, UHU). A spherical bead was used here instead of a sharp tip to average over a larger surface area with a well-defined contact geometry. The sample was placed in a Petri dish with the culture media and mounted on the temperature-controlled AFM stage. The cantilever was first positioned above the cell surface using a mechanical XY stage, and then the position was further adjusted using an XY piezo stage operated using a manipulation control option in the contact mode. Once positioned, illumination was switched off to minimise temperature fluctuations. The force measurements were performed at three values of force set point, 300, 500 and 1000 pN, and the cantilever travel speed was 0.5 μm/s operated in the closed loop mode to minimise hydrodynamic contributions (42). The cantilever spring constant was calibrated using the thermal fluctuation method (43). The typical values of spring constant were 0.04 N/m. The force data were pre-processed using using JPK software to perform baseline subtraction. Indentation force (F) and depth (D) data were then exported and fitted using MATLAB (R2016) to obtain an apparent Young's modulus (E). The Young's Modulus was determined using the classical Hertz contact model (44).

$$F = \frac{4}{3}\frac{E}{(1-\nu^2)}\sqrt{RD^3} \tag{1}$$

F is the indentation force, D is indentation depth, R is the radius of the spherical bead, ν is the Poission ratio ($\nu = 0.4$) (45), and E is the apparent Young's modulus. This model, which describes indentation of elastic solid objects by a spherical indentor, has been widely used to determine elasticity in cell mechanics studies (45–47) .

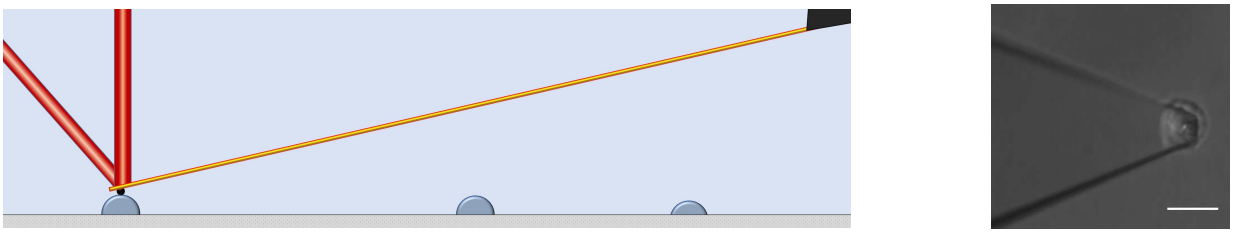

(a) (b)

Figure 1: AFM indentation. (a) Schematic setup for AFM measurements. (b) Cantilever with a bead attached at the tip for probing the nuclei. Scale bar - 10μm.

OT setup

Indentation experiments were carried out using an inverted microscope (Nikon Eclipse TE2000-U) with a 60x 1.2NA (Nikon, Plan Apo VC 60x WI) water immersion objective lens and a CCD camera (Andor Neo) to image and track beads. A Nd:Yag Laser (Spectra Physics) of power 1W at the laser head and a wavelength of 1064 nm was used to trap beads. A 2.5 mW probe laser (Thorlabs S1-FC-675) which is placed along the same beam path and focused at the QPD (Quadrant Photodiode) using the back focal plane of the condenser is used to detect the translations of a bead in a trap via a change in the interference pattern on the QPD. A piezo electric stage (PI P-517.3CD) was used to control precise stage displacements. Measurements were conducted at an ambient room temperature of T = 20°C. A sample chamber consisting of a polylysine coated coverslip and a welled microscope slide was prepared and filled with the loading medium and 2 μm diameter polystyrene beads (Poly Sciences Polystyrene 2.6% Solids latex, 0.001% suspension). A schematic of the Optical Tweezer (OT) setup and indentation procedure is presented in Fig. 2.

MCF7 nuclei were allowed to settle on the polylysine coated coverslip which was subsequently mounted on the piezo stage. Nuclei were laterally and longitudinally moved towards, and then into, an optically trapped bead as shown in the supplementary material (Movie - S1,S2). As the nucleus is indented the bead is displaced away from its equilibrium position in the optical trap. The position of the bead displacement when the nucleus is indented from the top is recorded using QPD data and image analysis with a centroid tracking algorithm simultaneously. An upwards displacement of the bead is indicated by the shift of the interference pattern on the QPD, registered by varying voltages from each quadrant and is also tracked using the standard deviation of the pixel intensity values from the image in the Region of Interest (ROI) around the particle. The conversion from standard deviation values to displacement was obtained by imaging a bead that was bound to a coverslip and moving the piezo

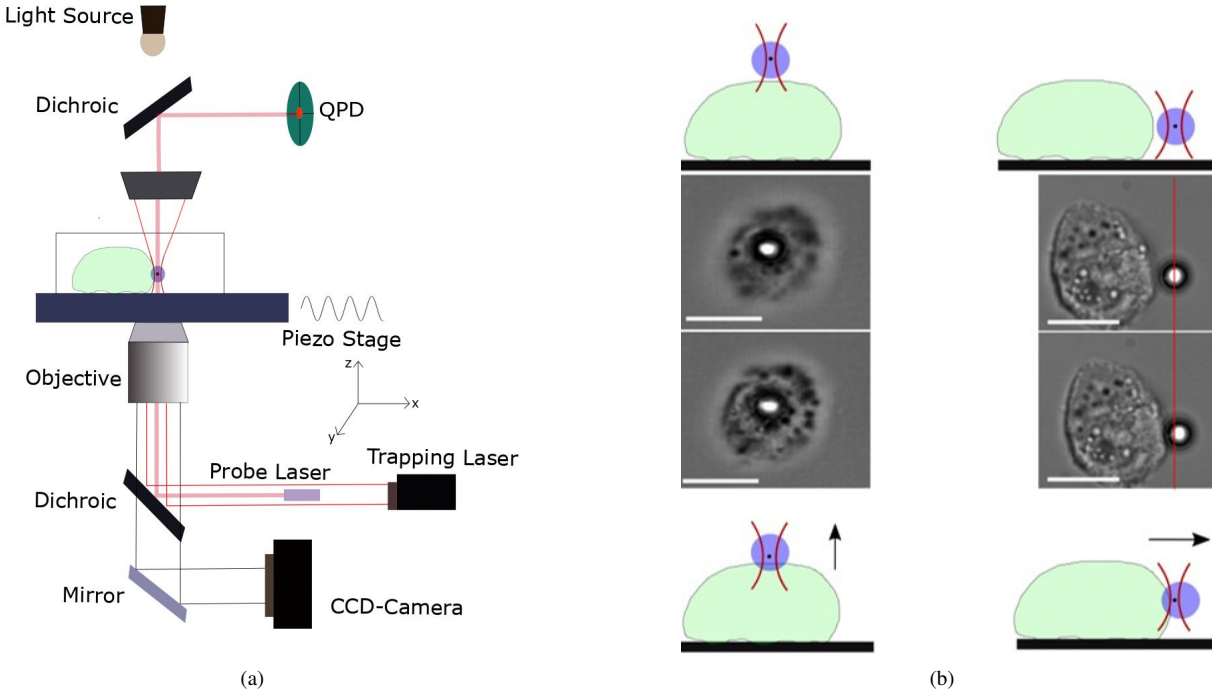

Figure 2: OT setup for nuclei indentation and force measurements in two directions, either approaching the nuclei from the top or from the side. (a) An infrared laser beam of wavelength 1064 nm is coupled into the optical path of a standard upright microscope via a dichroic mirror and focused into the sample by the objective. The stage position is controlled by a piezo stage. A probe laser of wavelength 675 nm placed in the same beam path and focused at the QPD detects the translations of bead in the trap. A CCD camera is used to acquire image sequences. (b) A nucleus is either moved towards the trapped bead longitudinally (from the top) or laterally (from the side) producing an indentation on the nuclei. The schematic of the experimental procedure shows the bead deflection. Scale bars - 5 μm.

stage in the z-direction with a 4 μm sinusoidal wave (Fig.S1). The QPD was also used to detect displacement perpendicular to the surface which is indicated by a change in the size of the interference pattern. However, as the probe laser passes through the nuclei, the interference pattern on the QPD is affected by the presence of nuclei. Although the QPD signal was nosier than that obtained from image analysis as a consequence of this, the absolute bead deflection measured was similar in both cases. The total displacement of the bead when indenting nuclei from the top is a combination of both longitudinal (perpendicular to the surface) and lateral (parallel to the surface) components of displacement. Hence, monitoring both the components gives the total force exerted on the bead by the nuclei, which leads to more accurate force measurements (Fig.S2).

The trap stiffness was calibrated in situ by using the power spectrum of the position signal of the trapped bead and applying the equipartition theorem. The laser power was fixed to 1 W at the source. The longitudinal spring constant obtained for this laser power was 28 pN/μm whereas the lateral spring constant (the trap strength resisting motion parallel to the surface, perpendicular to the direction of the propagation of the laser) was found to be 48 pN/μm for the same laser power (48).

Young's modulus calculation for optical tweezers (OT)

The apparent Young's modulus (E) was obtained from OT force-indentation measurements by using the Hertz contact model, as in the AFM experiments. However, owing to the considerably lower magnitude and range of forces applied in the OT experiment, which limits the exploration of the control variable space, fitting to the full functional form was not carried out in this case. Instead, an analysis procedure inspired by the work of Guz et al. (46) and Bacabac et al.(49) was used. In this methodology the indentation depth is written as a constant common indentation depth (D_o) plus a small varying indentation

and Eq. 1 is expanded as a Taylor series around D_o. Retaining only the first order term yields:

$$E = \frac{3(1-\nu^2)}{4\sqrt{D_o R}} S \tag{2}$$

In this work the bead radius was $R = 1$ μm, the Poisson ratio, ν, was 0.4 (45), and D_o was pragmatically set to 50 nm for each case (corresponding to a difference between the applied stage movement and indenter reponse of $\geq$ 10 nm as shown in Fig. 6), allowing the comparison of the moduli from different samples. $S = \frac{dF}{dD}$, which can be extracted from a simple linear fit to the selected region of the experimental force-indentation curve. It is worth noting that this chosen interval remained within the region of the linear relation between stage displacement and indentation. Analysis were performed using MATLAB (R2016).

Microaspiration setup

Micropipettes were fabricated from borosilicate glass capillaries (QF-100-50-7.5, Sutter Instruments) using a CO_2 laser pipette puller (P-2000, Sutter Instruments). The micropipettes had a (6.5 ± 0.5) μm inner diameter. To reduce adhesion, each pipette was immersed in a silanising agent (Sigmacote, Sigma Aldrich) for 1–2 s and left to air dry overnight in order to form a uniform surface coating at the tip.

The microaspiration instrumentation, shown in Fig. 3(a), has been previously described in (50, 51). During an experiment, a micropipette was backfilled (52) and immersed in an electrolyte bath filled with 3 mL 1× PBS. Once the pipette was affixed in place, 50 μL of a solution containing nuclei isolated from MCF7 cells was transferred to the electrolyte bath near the pipette tip. To begin each experiment a potential of 0.1 V and suction pressure (ΔP) of 25-200 mbar (2.5-20 kPa) was applied using the electrometer and pressure pump respectively. An electrical current between the electrodes (I) was recorded simultaneously with an optical microscopy video focused on the pipette tip (Fig. 3(d)). An aspiration event consisted of a MCF7 cell nucleus deforming and being completely drawn through the pipette tip. The current decreased as the nuclei entered the tip, and only recovered when the nuclei traversed the tip, clearing the ionic transport pathway.

Aspiration event times (ΔT) were typically 0.5-2 s. Each experiment was run for 60-90 s, during which multiple aspiration events were captured. The micropipette was replaced between experimental runs when it became obstructed or clogged. The optical microscopy videos were captured at 24 frames per second and the electrical signals at 300 Hz.

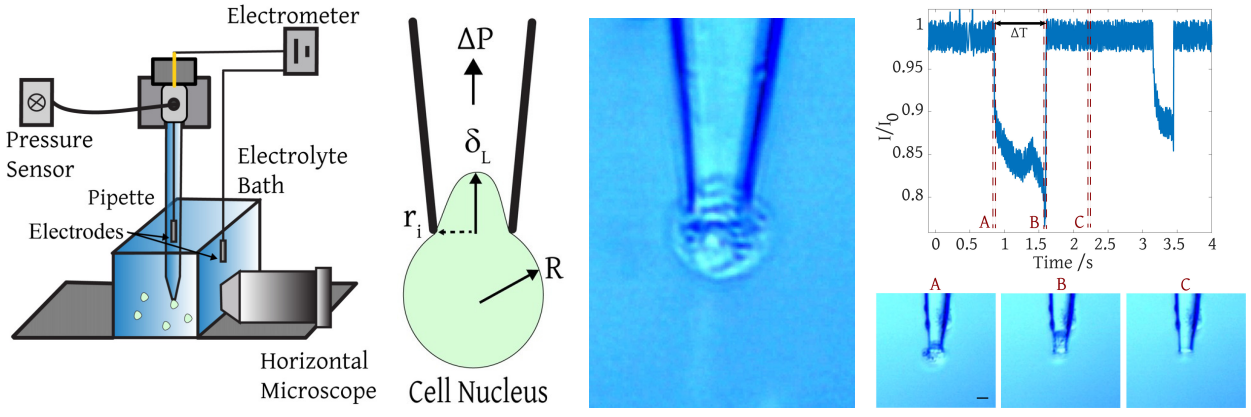

Figure 3: Microaspiration experiments and analysis. (a) Schematic setup for aspiration of MCF7 cell nuclei. (b) Schematic of the deformation parameters used for the solid elastic model (see text for definitions). (c) Example of the first frame showing aspiration of an MCF7 nucleus into a micropipette of inner diameter 6.5 ± 0.5 μm. (d) (Top) Example of an experimental current trace showing two aspiration events, and (Bottom) the corresponding video frames for the first event where frame **A** is the first frame of aspiration, frame **B** is the last frame of aspiration, and frame **C** is when no aspiration is occurring.

Two models were adopted to quantify cell nucleus mechanics. The first assumes that the deformed particle is an incompressible, elastic solid. Developed from micropipette aspiration studies (53, 54), this modified model has been detailed in (51), and relies solely on optical microscopy. When a nucleus starts to be aspirated it undergoes an initial elastic deformation, as shown in Fig. 3(b). Here R is the radius of the cell nucleus outside of the pipette, r_i is the pipette opening radius, δ_L is the initial

aspirated length, and ΔP is the pressure applied. δ_L is measured from optical microscopy using the first video frame in which the nucleus is aspirated into the micropipette tip (e.g. Fig. 3(d)). The effective elastic modulus (E') deduced using this model is

$$E' = \frac{r_i \Delta P}{\delta_L}. \tag{3}$$

The second model was developed for a viscoelastic particle (54). The data analysis method described previously (50) relies on the electrical signal (Fig. 3(d) (Top)). At the start of an experiment a baseline current (I_0) is established and measured. ΔT is defined as the time it takes for the nucleus to pass through the pipette tip constriction, measured as the time during which $I < 0.95 I_0$. Using the geometry of the pipette tip and the cell nucleus, a velocity for aspiration (u) can be estimated. The critical pressure required for aspiration to start, related to the surface tension of the cell nucleus, is assumed negligible compared to ΔP, and friction is also neglected in this analysis. The effective viscosity (η') of the nucleus is

$$\eta' = \frac{r_i \Delta P}{3\pi u}. \tag{4}$$

The viscous and elastic regimes are separated by a constant stress relaxation time (τ), and an effective elastic modulus (E') obtained using this second model is

$$E' = \frac{3\pi\eta}{\tau}. \tag{5}$$

The value $\tau = 0.3$ s was used for MCF7 nuclei, assumed to be the same as for MCF7 cells (55). For this model the corresponding video frames (Fig. 3(d) (Bottom)) are used to verify the timing of each aspiration event. Analysis were performed using MATLAB (R2016).

RESULTS AND DISCUSSIONS

HP1α knock-down results in softer nuclear periphery as determined by AFM force measurements

To explore if the reduction of HP1α alters the biophysical and biological properties of nuclei in malignant cells, MCF7 cells with constitutive KD of HP1α and a MCF7 control line were established. The reduction in HP1α expression in the MCF7 cells was confirmed by immunofluorescence microscopy using an antibody directed against HP1α. Fig. 4(a) shows distinct HP1α foci present in the nuclei of the MCF7 control cells that are absent in the nuclei of the HP1α KD cells. To determine if HP1α KD alters the malleability of the nuclear periphery, nuclei were isolated from the MCF7 cell lines for the mechanical measurements as described in Materials and Methods. The integrity of the isolated nuclei was confirmed using SEM, as shown in Fig. 4(b), the extraction procedure resulted in nuclei with little associated debris.

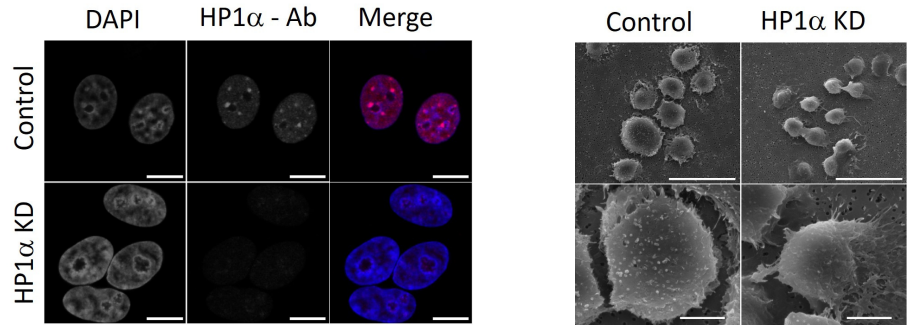

(a) (b)

Figure 4: Characterizations of nuclei. (a) Immunofluorescent confocal microscopy of MCF7 control (top panel) and MCF7 HP1α KD (bottom panel) cells stained with DAPI to detect DNA (*blue* in merge) and an antibody (Ab) directed against HP1α (*red* in merge). Scale bars - 10μm. (b) Representative scanning electron micrographs of nuclei isolated from the two cell lines. Scale bars : top panel - 30μm, bottom panel - 5μm.

Fig. 5 shows results obtained using AFM. Nuclei were indented at a constant rate of 0.5 μm/s and three sweeps were performed between zero and maximum forces of 300 pN (*black* circle), 500 pN (*green* circle) and 1nN (*blue* circle). The indentation and the retraction curves were similar, suggesting that the response was highly reversible and hence can be considered

to be consistent with largely elastic behaviour. A clear difference can be observed in the force-indentation curve between the control and HP1α KD nuclei. The magnitude of the indentation for HP1α KD nuclei is about an order of magnitude higher than for control nuclei signifying that the periphery of the HP1α KD nuclei are comparatively softer than those of the control nuclei.

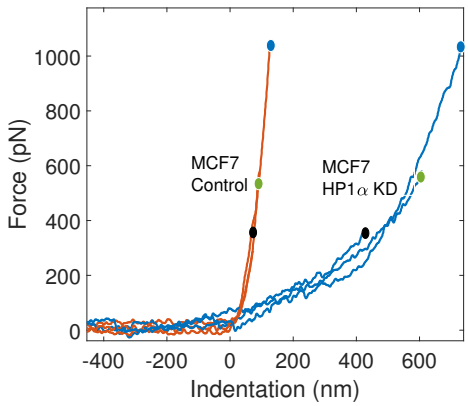

Figure 5: AFM indentation : Three sweeps were applied between zero and maximum forces of 300 pN (*black* circle), 500 pN (*green* circle) and 1000 pN (*blue* circle) on MCF7 control and HP1α KD nuclei. The Hertzian fit to the force-indentation curve is shown in Fig.S3.

Indentation performed by nN-scale forces is likely to induce damage and may have an effect on the measured modulus and were not pursued. Measuring forces below $\sim$ 30 pN was not possible in these AFM experiments due to the thermal fluctuations of the AFM cantilever in liquid setting a limit below which force could not be measured and the absolute indentation becomes impossible to assess. To have an absolute estimate of indentation at forces below 30 pN, OT were implemented.

HP1α knock-down results in softer nuclear periphery as determined by OT

To measure deformations at low forces, OT were used to perform indentation of the nuclear periphery by laterally (from the side, parallel to the surface) and longitudinally (from the top, perpendicular to the surface, as in an AFM experiment) moving the MCF7 nuclei against optically trapped micro-beads and measuring the bead displacement as shown in Fig. 6. When the trapped bead is pushed into the nuclei, the apparent Young's modulus can be estimated using the Hertzian contact model as described in Materials and Methods. The same size bead (2 μm diameter) and the same deformation rate (0.5 μm/s) as applied in the AFM measurements were used, in order for the experiments to be as comparable as possible.

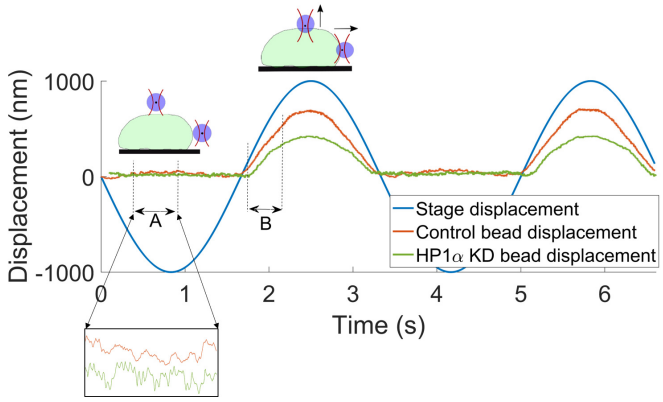

Figure 6: Stage and bead displacements. Stage displacement is represented by the *blue* curve. MCF7 control and HP1α KD nuclei are represented by *red* and *green* curve respectively. Trap stiffness is calculated from interval A, where the bead is freely diffusing in the optical trap. The indentation on the nuclei is extracted by linearly fitting the region of interval B.

Fig. 6 shows the sweeping, sinusoidal movement of the stage during experiments. The trap stiffness is measured *in situ* during the first half of the sinusoidal period, when the nucleus is far away from the optically trapped particle and the bead is

freely diffusing in the trap. This is shown in the inset for the interval A in Fig. 6. The interaction between a single nucleus and a bead is observed in the second half of each sinusoid, whereupon the nucleus is driven into the optically trapped bead. Bead displacement is measured as described in the Materials and Methods. Once the trap stiffness (k) and bead displacement (BD) are known, Hooke's law is used to estimate the restoring force generated ($F = -kBD$). When the nucleus comes into contact with the bead and begins to push it, bead displacement (BD) increases in the same direction as piezo stage displacement (SD). The difference between the displacement of the stage (and thus nucleus) and the resultant displacement of the trapped bead gives the indentation ($D = SD - BD$). Region B in Fig. 6 represents the indentation, where the linear region is used to estimate the elastic modulus as described in Materials and Methods.

To investigate potential anisotropy in the mechanical properties of the nuclear periphery, nuclei were indented both laterally and longitudinally in relation to the surface. Nuclei having a semi-spherical shape (as opposed to substantially spread on the surface to which they are attached) are able to be indented laterally as shown in Fig. 2(b). This lateral indentation avoids potential laser-induced local heating that is present for longitudinal indentation, when the laser passes through the nuclei (56). The interference pattern on the QPD is also significantly affected as the laser does not pass through the nuclei, manifesting better QPD-derived data when compared to that obtained from longitudinal indentation.

From the temporal sequences for the indentation intervals shown in Figs. 7(a), 7(b), 7(d) and 7(e), force-indentation curves similar to AFM were obtained (compare Figs. 7(c) and 7(f) with Fig 5). Consistent with the AFM experiments, the periphery of MCF7 nuclei with HP1α KD have greater indentation compared to the control nuclei for the same applied force. The slope of the force-indentation plot is used to estimate Young's modulus using equation 2. Using the OT method, we can clearly distinguish forces as low as 1 pN, which allows a more accurate estimate of mechanical properties of the nuclear periphery in the range from 1 to 10 pN in comparison with AFM experiments. Table 1 gives the maximum indentation for both types of nucleus using lateral and longitudinal indentation methods. The average indentation for the two indentation methods is similar, giving confidence in both methods and showing that there is probably little effect of any anisotropy. The periphery of the MCF7 control nuclei have smaller indentations compared to HP1α KD nuclei, suggesting that reduced expression of HP1α makes nuclear periphery softer.

Table 1: Maximum indentation

Method of Indentation	Control nuclei	HP1α KD
Longitudinal (nm)	105 ± 31	359 ± 137
Lateral (nm)	123 ± 61	351 ± 79

Along with probing isolated MCF7 nuclei, mechanical measurements of whole MCF7 cells were carried out using OT for both control and HP1α KD . The apparent Young's modulus distributions, as shown in supplementary figure (Fig.S5), confirm that the whole cells are affected by the KD in a similar way to the isolated nuclei. As expected, the whole HP1α KD cells show a slightly higher modulus ((64±27) Pa) as compared to those of isolated nuclei (longitudinal (54±26) Pa, lateral (40±24) Pa), most likely owing to the properties of the cytoskeleton (Fig.S6) above the nucleus in both control and HP1α KD cells. A maximum intensity projection of z stack images of the cell obtained from confocal microscopy (Fig.S6) show that while nuclei (*blue*) are by far the largest organelle in MCF7 cells, there is indeed a small layer of cytoskeleton between the nuclei and cell membrane.

Comparison of force-indentation plot and elastic modulus using OT and AFM

AFM provides insight into the mechanical properties of the nuclei at larger forces (~1 nN) than used for OT. However, OT gives better measurements of the absolute indentation for lower forces (~10 pN) at which AFM measurements are limited by the thermal noise of the cantilever in liquid. In Fig. 8, it can be seen that the cantilever noise is around 50 ± 30 pN, which is roughly the maximum force exerted in our OT setup.

The distributions of repeated elastic modulus measurements for the periphery of the MCF7 control and HP1α KD nuclei obtained using AFM and OT are shown in Fig. 9 in box plot distributions. For OT, experiments were carried out on 22 nuclei (lateral indentation) and 12 nuclei (longitudinal indentation). For AFM, experiments were conducted on 17 nuclei from both MCF7 control and HP1α KD cells. A difference in the elastic modulus of the nuclear periphery between control and HP1α KD can be observed using either AFM or OT, ($p < 0.0001$). Fig.9(b) shows the Young's modulus obtained for a maximum force of 0.5nN. Similar AFM experiments were carried out for a maximum force of 0.3nN and 1nN (Fig.S4). These results are consistent with previous studies on differences of nuclei mechanics extracted from benign (MCF-10A) and malignant (MCF-7) cells (34) .

The apparent Young's moduli of the nuclear periphery of control nuclei have a larger spread of values, signifying that the structure of the MCF7 control nuclei are more mechanically heterogeneous in nature compared to the HP1α KD. For the

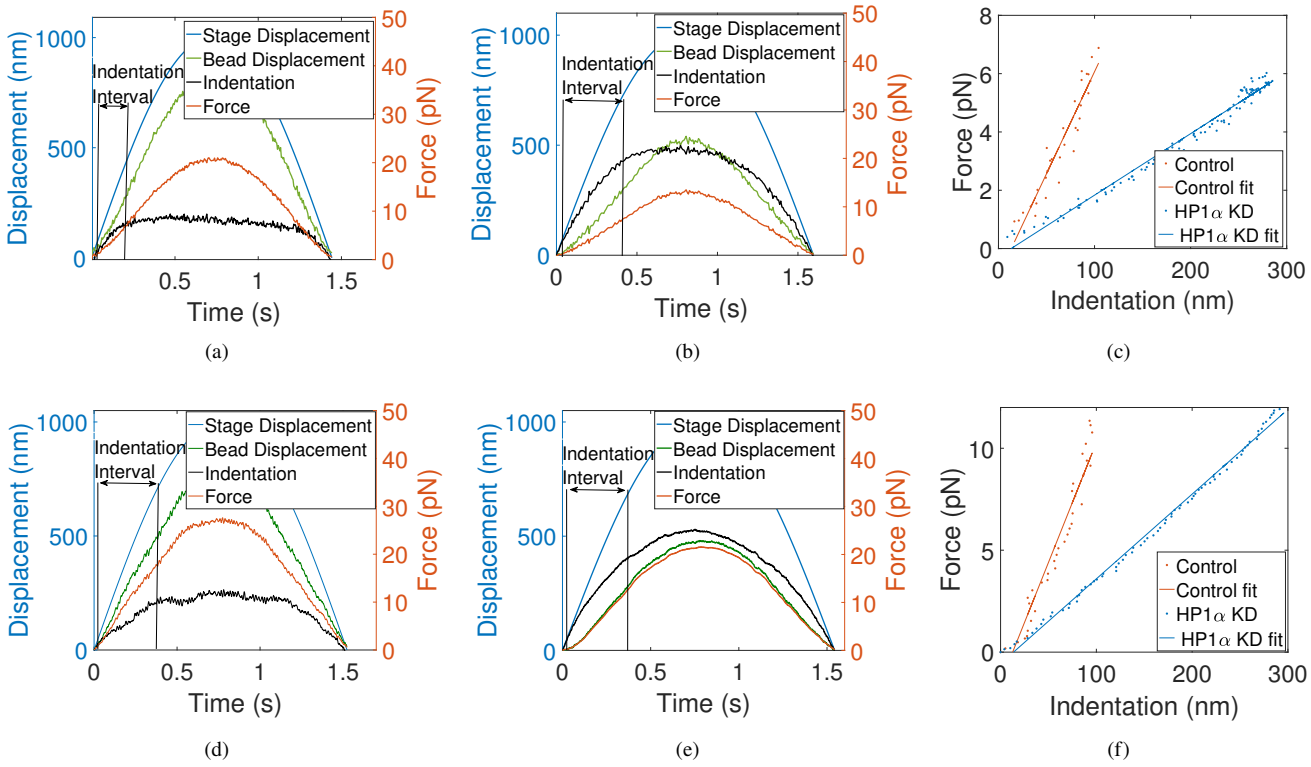

Figure 7: **Longitudinal** (from the top) indentation: (a) and (b) represents the measured bead displacement (*green*), calculated force (*red*) and indentation (*black*) during the indentation interval, when the bead interacts with MCF7 control and HP1αKD nuclei respectively. (c) Force-indentation curves extracted from the indentation interval. **Lateral** (from the side) indentation: (d) and (e) represents the measured bead displacement (*green*), calculated force (*red*) and indentation (*black*) during the indentation interval, when the bead interacts with MCF7 control and HP1αKD nuclei respectively. (f) Force-indentation curves extracted from the indentation interval.

same loading rate (0.5 μm/s), the apparent elastic moduli determined using OT are much smaller than AFM values. A similar difference in modulus measured by AFM and OT has been reported for MC3T3-E1 osteoblasts and MLO-Y4 osteocytes cells isolated from fetal chicken calvariae (45, 49). The difference is mainly due to the vast difference in the magnitude of forces applied as shown in Fig. 8. The OT are capable of measuring an apparent modulus at an indentation length for which AFM is unable to conclusively report that contact has been made.

Nuclei from HP1α knock-down and control cells have similar bulk properties as determined by MA experiments

MA measurements are different in nature from OT and AFM because the test involves deformation of the whole nucleus as opposed to the local deformations of the nuclear periphery that are imposed by OT and AFM. Much greater forces and strains are applied, and deformation includes the bulk of the chromatin interior. In contrast, only a small area of the nuclear periphery is locally deformed when using a micron-sized indenter bead, so that the results obtained for effective Young's modulus from MA (Fig. 10) are not expected to be directly comparable to OT and AFM data. The values obtained in Fig. 10 can be seen to lie between those obtained using OT and AFM in Fig. 9. The apparent Young's moduli for the two types of nuclei are similar (2.2 ± 0.3 kPa for the control, 3.9 ± 0.6 kPa for the HP1α KD), but slightly larger ($p < 0.05$) for the nuclei extracted from the HP1α KD cells.

A likely explanation for this difference involves deformation of the bulk, and it is possible that the bulk mechanical properties of HP1α KD nuclei are a little higher than those for control nuclei (in contrast to the results for the periphery). Support for this possibility is provided by Stephens et al.'s recent study of nuclear mechanics (20). These researchers concluded that chromatin affects short extensions (< 3 μm, or 30% strain), while lamina in the bulk of the nucleus affects larger extensions to a larger degree. They also noted that the core-membrane structure can affect the mechanics, and suggested that this could cause apparent

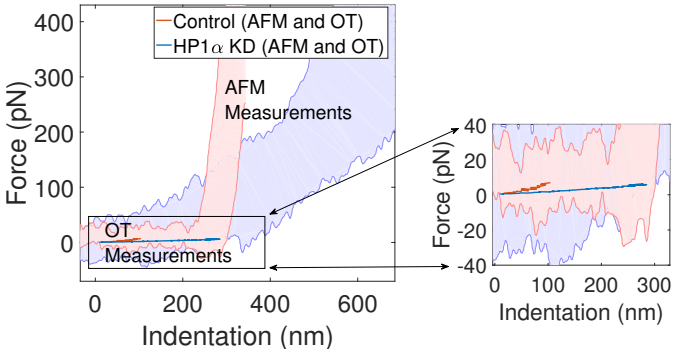

Figure 8: Comparison of the noise in the force indentation plots for control and HP1α KD nuclei using AFM and OT.

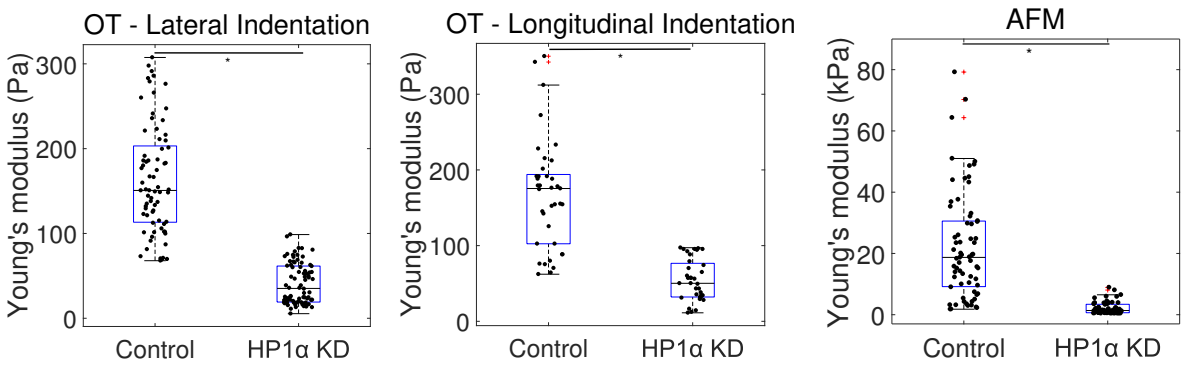

Figure 9: Box plot representation of Young's modulus values measured using OT and AFM (*$p < 0.0001$). (a) Young's modulus obtained for lateral (from the side) and longitudinal (from the top) indentation using OT ($n = 73$ (control - lateral indentation), 64 (HP1α KD - lateral indentation), 38 (control - longitudinal indentation), 32 (HP1α KD - longitudinal indentation)). (b) Young's modulus obtained using AFM data for a maximum force of 0.5 nN ($n = 67$ (control), 64 (HP1α KD)). The 'n' indicates total number of indentations performed to obtain modulus values.

strain-hardening.

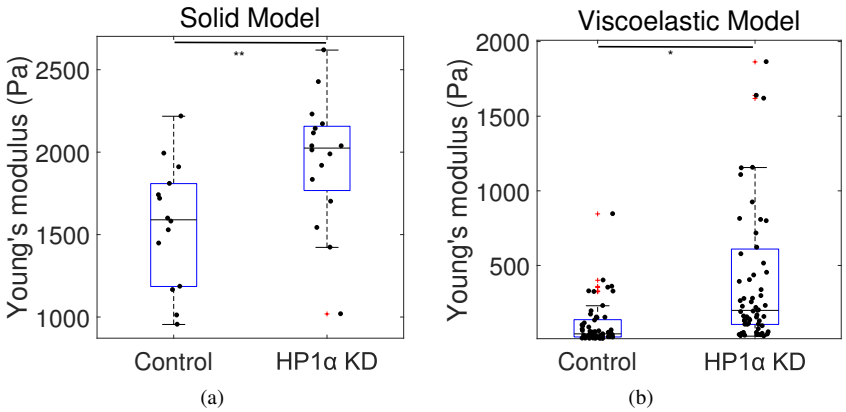

Figure 10: Effective Young's modulus from microaspiration experiments. (a) Values obtained using the solid model (Eq. 3, **$p < 0.01$) ($n = 14$ (control), 16 (KD)). (b) Values obtained using the viscoelastic model (Eq. 5, *$p < 0.05$) ($n = 61$ (control), 67 (KD)) .

It is worth revisiting the two models used to obtain the data shown in Fig. 10 for the MA experiments, both of which give values that are intermediate between the AFM and OT results. Data obtained using the solid model are greater, and closer to the AFM values. This may be because the solid model only analyses small, initial deformations that may be less affected by the bulk properties of the nuclei. In contrast, the viscoelastic model uses the entire duration of the deformation, and incorporates stress relaxation. The differences in the extracted parameters demonstrate that in order to compare mechanical measurements obtained from nuclei and cells, attention has to be paid to the details of the analysis methodology, and not just the experimental technique.

HP1α knock-down alters heterochromatin and nuclear lamina organisation

Electron micrographs of HP1αKD nuclei show a difference in the patterning of the heterochromatin when HP1α expression is reduced (Fig. 11(a)). The MCF7 control cells have characteristic electron dense regions of heterochromatin and lighter regions of euchromatin, while the pattern of chromatin is more homogeneous in the HP1α KD cells (Fig. 11(a)). Domains of heterochromatin are marked by di- and tri-methylation of lysine 9 on core histone H3 (H3K9me2/3) (6). To identify if HP1α KD disrupts the level and localisation of these heterochromatin marked domains, firstly, histones were extracted from the MCF7 control and HP1α KD nuclei and immunoblot analysis performed to determine the level of H3K9me2 and H3K9me3. Compared to the control cells there is a reduction in the level of both H3K9me2 and H3K9me3 in the HP1α KD line (Fig. 11(b)). As lamina-associated heterochromatin domains are enriched in H3K9me2 (57), its distribution at the nuclear periphery was explored (Fig. 11(c)). While there is a distinct layer of H3K9me2 marked heterochromatin adjacent to the Lamin A/C network

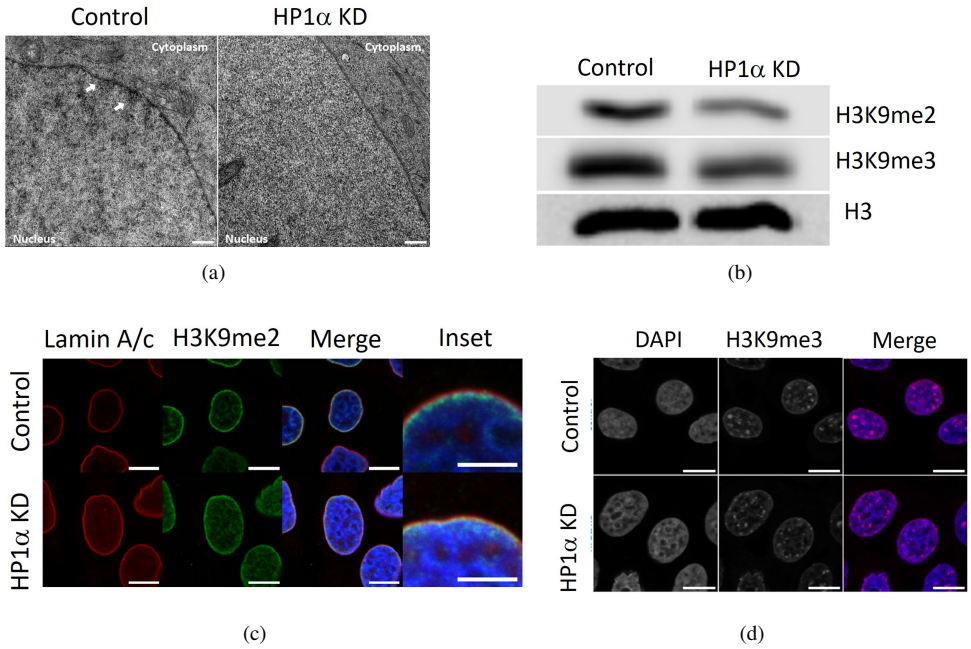

Figure 11: Knockdown of HP1α disrupts chromatin organization in MCF7 cells. (a) Representative electron micrographs showing regions of compact heterochromatin at the nuclear periphery in MCF7 control cells (*white* arrows), while the nuclei of MCF7 HP1αKD cells have a more diffuse chromatin patterning. Scale bars - 500 nm. (b) Immunoblot analysis of extracted histones from MCF7 control and HP1α KD cells probed with antibodies raised against markers of heterochromatin; dimethylation of lysine 9 on histone H3 (H3K9me2) and trimethylation of lysine 9 on histone H3 (H3K9me3). An antibody against histone H3 is used as a loading control. (c) Representative immunofluorescence confocal microscopy images of MCF7 control and MCF7 HP1α KD cells stained with DAPI to detect DNA (*blue*) and antibodies against H3K9me2 (*green*) and Lamin A/C (*red*). Scale bars - 10 μm, inset - 5 μm. (d) Representative immunofluorescence confocal microscopy images of MCF7 control and MCF7 HP1α KD cells stained with DAPI to detect DNA (*blue*) and an antibody to detect H3K9me3 (*red*). Scale bars - 10 μm.

in the control cells, a more diffuse distribution of H3K9me2 lines the Lamin A/C network in nuclei lacking HP1α. This more diffuse distribution is also observed on the bulk of the chromatin in the HP1α KD nuclei. Heterochromatin foci marked by H3k9me3 that represent chromocenters are still present in cells with reduced expression of HP1α, however they appear smaller

and more dispersed than the distinct punctate foci of H3K9me3 chromatin in the MCF7 control cells (Fig. 11(d)). This more homogeneous chromatin organisation and disruption to the peripheral heterochromatin in HP1α KD nuclei is consistent with the reduced variation in the spread of mechanical values for these nuclei.

To identify if the loss of heterochromatin integrity upon HP1α KD also disrupted the nuclear lamina, the lamin networks were visualised by immunofluorescence confocal microscopy. Fig. 12(a) shows that the Lamin A/C network is more crumpled and irregular in HP1α KD cells compared to those of the MCF7 control cells. While there is less disruption to the Lamin B2 layer (Fig. 12(b)), an increase in punctate foci is also observed in nuclei with HP1α KD indicating that there is an increased invagination of the Lamin B network in these cells. To determine if this altered morphology of the nuclear lamina is due to changes in the expression or localisation of the lamins, cell fractions were prepared from MCF7 control and HP1α KD cells, and analysed by immunoblotting with antibodies against Lamin A/C and Lamin B2 (Fig. 13). While there is no difference in the amount of lamins present in either whole cell or nuclear fractions from MCF7 control and HP1α KD cells, there is a reduction in the amount of Lamin A/C (Fig. 13(a)) and Lamin B2 (Fig. 13(b)) present in the nuclear envelope fraction of HP1α KD cells. As this suggests that the lamins are more stably integrated into the nuclear lamina of the MCF7 control cells, biochemical extractions were performed where isolated nuclei from the MCF7 control and HP1α KD cells were sequentially extracted with increasing concentrations of salt as described in Materials and Methods (Fig. 14). The supernatents and insoluble pellets were then analysed by immunoblotting with antibodies against Lamin A/C and Lamin B2. Fig. 14(a) demonstrates that more Lamin A/C was extracted from the HP1α KD nuclei by 150 mM and 250 mM NaCl than in the control cells. Similarly, more Lamin B2 was extracted from HP1α KD cells at lower molarities of NaCl (Fig. 14(b)), suggesting both A-type and B-type lamins are more tightly associated with the nuclear lamina in the MCF7 control cells. Interestingly, this disruption to the nuclear lamina in MCF7 HP1α KD cells was not observed in previous studies when the overall level of heterochromatin was reduced through the expression of HMGN5 or treatment with HDAC inhibitors (19, 25).

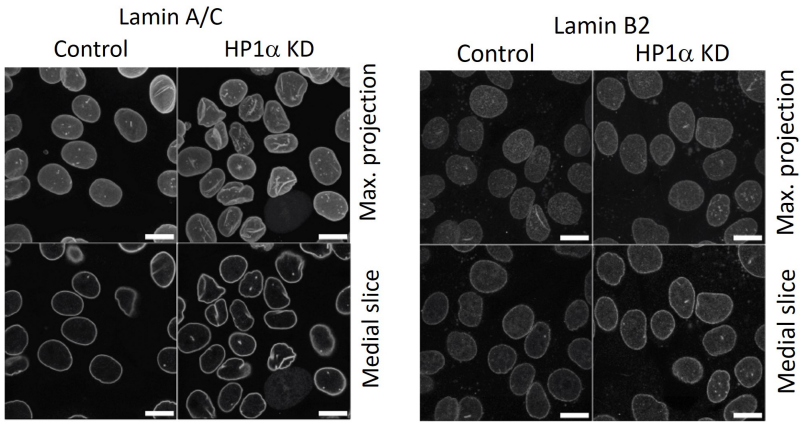

Figure 12: Knock-down of HP1α alters the morphology of the lamin network. Immunofluorescence confocal microscopy of MCF7 control and MCF7 HP1α KD cells probed with (a) an antibody against Lamin A/C or (b) an antibody against Lamin B2 to determine changes in nuclear lamina morphology. Representative images of maximum intensity projection of z stack (top panel) or a medial slice (bottom panel) are shown. Scale bars - 10μm.

In summary, the reduction of HP1α alters global chromatin organisation. Electron micrographs show a more homogenous distribution of chromatin in MCF7 cells with HP1α KD. Heterochromatin foci marked with H3K9me2/3 are present in these cells, although the overall levels of these marks are reduced. The dispersed domains of heterochromatin marked by H3K9me2 at the nuclear periphery, likely reflect a decrease in the tethering of heterochromatin to the nuclear envelope/lamina due to loss of the interaction of HP1α with LBR and PRR14 (9–11, 22). The nuclear lamina was also disrupted with the reduction of HP1α in MCF7 cells. While the level of lamin expression is unchanged, reduction of HP1α, given its role in gene silencing, could be disrupting the integrity of the lamina by altering the activity of pathways that regulate lamin dynamics. Reduced tethering of peripheral heterochromatin to the nuclear lamina could also be contributing by distorting the post-mitotic assembly of the lamina and nuclear envelope (58, 59).

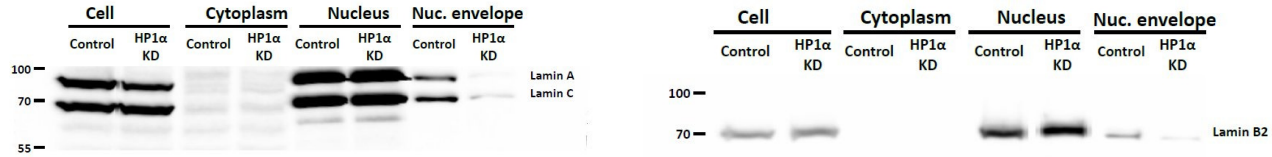

(a) (b)

Figure 13: Knockdown of HP1α in MCF7 cells disrupts the nuclear lamina. Levels of lamin expression and localisation in whole and fractionated cell lysates from an equal number of MCF7 control or HP1α KD cells were analysed by immunoblotting. (a) Immunoblot probed with an antibody against Lamin A/C. (b) Immunoblot probed with an antibody against Lamin B2.

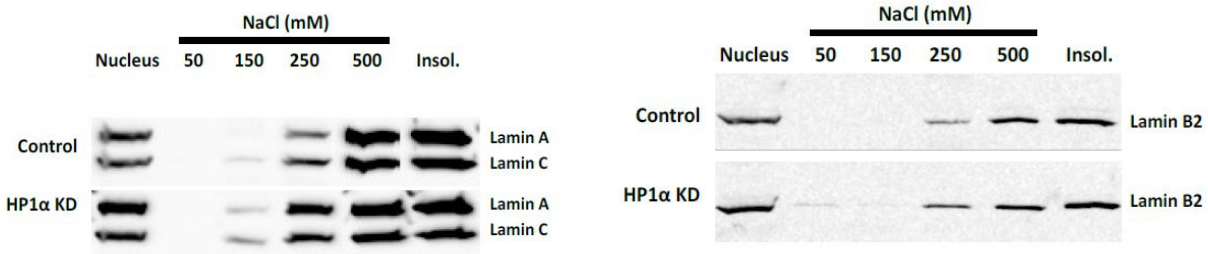

(a) (b)

Figure 14: Increased extractability of lamins in HP1α KD cells. Immunoblot analysis of isolated nuclei of MCF7 control (top panel) or MCF7 HP1α KD (bottom panel) cells extracted with increasing concentrations of NaCl, and the remaining insoluble (Insol.) fraction. (a) Immunoblot probed with an antibody against Lamin A/C. (b) Immunoblot probed with an antibody against Lamin B2.

CONCLUSION

In this paper, we have studied the mechanical properties of nuclei isolated from malignant MCF7 cells with constitutive KD of HP1α expression using three mechanical measurement techniques which deform the nuclei in very different ways. They probe the nuclear periphery ($\sim$ 100 nm) with forces on scales of 10 pN (OT) or 1 nN (AFM); and the bulk properties with whole-of-nuclei deformations (MA). While OT and AFM both probe the nuclear periphery, AFM experiments were carried out at higher forces as compared to OT and care must be taken when interpreting the absolute indentation (49). Absolute values of Young's modulus obtained using these three techniques are not in close agreement, as might be expected (60). This highlights that mechanical measurements carried out on nuclei are difficult because they are viscoelastic and heterogeneous. In addition, models used to derive apparent moduli from experiments often assume linear elasticity.

Despite the inherent approximations of the analysis, data from indentation techniques (AFM and OT) demonstrate that there is a significant decrease in the apparent Young's modulus of the nuclear periphery from MCF7 HP1α KD cells as compared to control nuclei reflecting the altered organisation of the peripheral heterochromatin and the lamin networks observed in these nuclei Fig. 15(a). In contrast the bulk moduli obtained by MA show little difference, indicating a situation where the overall integrity of the nucleus is likely maintained while the softening of the nuclear periphery enhances migration.

More specifically the disruption to the nuclear periphery upon HP1α KD correlates with the reduced elastic modulus of the periphery of the HP1α KD nuclei. Considering the higher magnitude of forces applied by AFM compared with OT, it is likely that the higher apparent magnitude of the moduli originates from engaging more of the underlying lamina shell in the more extreme local deformation. In contrast, OT is mostly probing the very outside of the nuclear periphery and is capable of reporting absolute indentations at much lower forces (Fig. 8). AFM might be indenting and stretching the lamina and chromatin beneath the nuclear membrane. In this scenario, the AFM elastic force is proportional to the in-plane modulus of the lamina - chromatin envelope and the stretch factor (which is some function of delta, lamina layer thickness, probe radius etc) (Fig. 15(b)).

The altered mechanical properties of these nuclei reinforces the central role heterochromatin homeostasis plays in the physical integrity of nucleus. Therefore, loss of HP1α in malignant cells, given its role in the spatial organisation of the genome not only aids malignant cell invasion through changes in gene expression, but physically by increasing the malleability of the

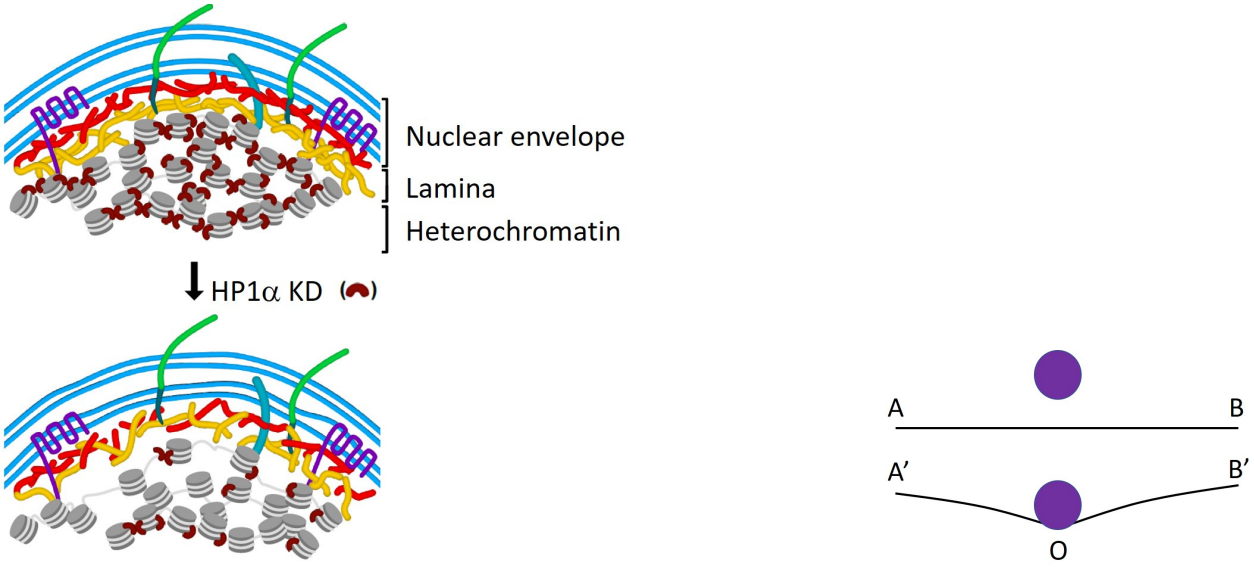

(a) (b)

Figure 15: (a) Schematic diagram showing the disruption to the nuclear periphery when HP1α expression is reduced. Loss of HP1α disturbs the organisation of heterochromatin, disrupting its tethering to the nuclear lamina and causing a change in the morphology and dynamics of the lamina. These changes result in a nucleus with a more malleable shell. (b)AFM probes lamin stretching. A'OB' = AB + 2*delta, where delta is the stretch.

nucleus without causing a loss of integrity.

AUTHOR CONTRIBUTIONS

Experimental work and data analyses was carried out by SP (OT, AFM, MA); RS,TKH (Cell maintenance, nuclei extraction, microscopy and biochemical assays); AG (MA); and GEY (AFM). All authors contributed to the planning of the work, the interpretation and the writing of the manuscript.

ACKNOWLEDGMENTS

SP, AG, GW, CW and MAKW would like to thank the MacDiarmid Institute for support. MMIC is acknowledged for help with microscopy. Prof Jason Stokes is thanked for facilitating visits to Queensland. RS and TKH were supported by grants from the Health Research Council of New Zealand Breast Cancer Research Grant and the Palmerston North Medical Research Foundation.

SUPPLEMENTARY MATERIAL

Supporting material contains five figures and two movies.

REFERENCES

1. Kumar, Y., D. Sengupta, and W. Bickmore, 2020. Recent advances in the spatial organization of the mammalian genome. *J Biosci* 45. https://www.ncbi.nlm.nih.gov/pubmed/31965996.

2. Dechat, T., K. Pfleghaar, K. Sengupta, T. Shimi, D. K. Shumaker, L. Solimando, and R. D. Goldman, 2008. Nuclear lamins: major factors in the structural organization and function of the nucleus and chromatin. *Genes Dev* 22:832–853. https://www.ncbi.nlm.nih.gov/pubmed/18381888.

3. Shimi, T., K. Pfleghaar, S. Kojima, C. G. Pack, I. Solovei, A. E. Goldman, S. A. Adam, D. K. Shumaker, M. Kinjo, T. Cremer, and R. D. Goldman, 2008. The A- and B-type nuclear lamin networks: microdomains involved in chromatin organization and transcription. *Genes Dev* 22:3409–3421. https://www.ncbi.nlm.nih.gov/pubmed/19141474.

4. Holaska, J. M., K. L. Wilson, and M. Mansharamani, 2002. The nuclear envelope, lamins and nuclear assembly. *Curr Opin Cell Biol* 14:357–364. https://www.ncbi.nlm.nih.gov/pubmed/12067659.

5. Pombo, A., and N. Dillon, 2015. Three-dimensional genome architecture: players and mechanisms. *Nat Rev Mol Cell Biol* 16:245–257. https://www.ncbi.nlm.nih.gov/pubmed/25757416.

6. Janssen, A., S. U. Colmenares, and G. H. Karpen, 2018. Heterochromatin: Guardian of the Genome. *Annu Rev Cell Devel Biol* 34:265–288. https://www.ncbi.nlm.nih.gov/pubmed/30044650.

7. Grewal, S. I., and S. Jia, 2007. Heterochromatin revisited. *Nat Rev Genet* 8:35–46. http://www.ncbi.nlm.nih.gov/entrez/query.fcgi?cmd=Retrieve&db=PubMed&dopt=Citation&list_uids=17173056.

8. Ryan, D. P., and D. J. Tremethick, 2018. The interplay between H2A.Z and H3K9 methylation in regulating HP1alpha binding to linker histone-containing chromatin. *Nucleic Acids Res* 46:9353–9366. https://www.ncbi.nlm.nih.gov/pubmed/30007360.

9. Polioudaki, H., N. Kourmouli, V. Drosou, A. Bakou, P. A. Theodoropoulos, P. B. Singh, T. Giannakouros, and S. D. Georgatos, 2001. Histones H3/H4 form a tight complex with the inner nuclear membrane protein LBR and heterochromatin protein 1. *EMBO Rep* 2:920–925. http://www.ncbi.nlm.nih.gov/entrez/query.fcgi?cmd=Retrieve&db=PubMed&dopt=Citation&list_uids=11571267.

10. Kourmouli, N., G. Dialynas, C. Petraki, A. Pyrpasopoulou, P. B. Singh, S. D. Georgatos, and P. A. Theodoropoulos, 2001. Binding of heterochromatin protein 1 to the nuclear envelope is regulated by a soluble form of tubulin. *J Biol Chem* 276:13007–13014. https://www.ncbi.nlm.nih.gov/pubmed/11278332.

11. Poleshko, A., K. M. Mansfield, C. C. Burlingame, M. D. Andrake, N. R. Shah, and R. A. Katz, 2013. The human protein PRR14 tethers heterochromatin to the nuclear lamina during interphase and mitotic exit. *Cell reports* 5:292–301. http://www.ncbi.nlm.nih.gov/pubmed/24209742.

12. Carone, D. M., and J. B. Lawrence, 2013. Heterochromatin instability in cancer: from the Barr body to satellites and the nuclear periphery. *Seminars in cancer biology* 23:99–108. http://www.ncbi.nlm.nih.gov/pubmed/22722067.

13. Bank, E. M., and Y. Gruenbaum, 2011. The nuclear lamina and heterochromatin: a complex relationship. *Biochem Soc Trans* 39:1705–1709. http://www.ncbi.nlm.nih.gov/pubmed/22103511.

14. Mekhail, K., and D. Moazed, 2010. The nuclear envelope in genome organization, expression and stability. *Nat Rev Mol Cell Biol* 11:317–328. http://www.ncbi.nlm.nih.gov/pubmed/20414256.

15. Mellad, J. A., D. T. Warren, and C. M. Shanahan, 2011. Nesprins LINC the nucleus and cytoskeleton. *Current opinion in cell biology* 23:47–54. http://www.ncbi.nlm.nih.gov/pubmed/21177090.

16. Bustin, M., and T. Misteli, 2016. Nongenetic functions of the genome.

17. Swift, J., I. L. Ivanovska, A. Buxboim, T. Harada, P. C. Dingal, J. Pinter, J. D. Pajerowski, K. R. Spinler, J. W. Shin, M. Tewari, F. Rehfeldt, D. W. Speicher, and D. E. Discher, 2013. Nuclear lamin-A scales with tissue stiffness and enhances matrix-directed differentiation. *Science* 341:1240104. https://www.ncbi.nlm.nih.gov/pubmed/23990565.

18. Lammerding, J., L. G. Fong, J. Y. Ji, K. Reue, C. L. Stewart, S. G. Young, and R. T. Lee, 2006. Lamins A and C but not lamin B1 regulate nuclear mechanics. *J Biol Chem* 281:25768–25780. https://www.ncbi.nlm.nih.gov/pubmed/16825190.

19. Furusawa, T., M. Rochman, L. Taher, E. K. Dimitriadis, K. Nagashima, S. Anderson, and M. Bustin, 2015. Chromatin decompaction by the nucleosomal binding protein HMGN5 impairs nuclear sturdiness. *Nat Commun* 6:6138. https://www.ncbi.nlm.nih.gov/pubmed/25609380.

20. Stephens, A. D., E. J. Banigan, S. A. Adam, R. D. Goldman, and J. F. Marko, 2017. Chromatin and lamin A determine two different mechanical response regimes of the cell nucleus. *Mol Biol Cell* 28:1984–1996. https://www.ncbi.nlm.nih.gov/pubmed/28057760.

21. Harr, J. C., T. R. Luperchio, X. Wong, E. Cohen, S. J. Wheelan, and K. L. Reddy, 2015. Directed targeting of chromatin to the nuclear lamina is mediated by chromatin state and A-type lamins. *J Cell Biol* 208:33–52. https://www.ncbi.nlm.nih.gov/pubmed/25559185.

22. Solovei, I., A. S. Wang, K. Thanisch, C. S. Schmidt, S. Krebs, M. Zwerger, T. V. Cohen, D. Devys, R. Foisner, L. Peichl, H. Herrmann, H. Blum, D. Engelkamp, C. L. Stewart, H. Leonhardt, and B. Joffe, 2013. LBR and lamin A/C sequentially tether peripheral heterochromatin and inversely regulate differentiation. *Cell* 152:584–598. http://www.ncbi.nlm.nih.gov/pubmed/23374351.

23. Dahl, K. N., A. J. Engler, J. D. Pajerowski, and D. E. Discher, 2005. Power-law rheology of isolated nuclei with deformation mapping of nuclear substructures. *Biophys J* 89:2855–2864. http://www.ncbi.nlm.nih.gov/pubmed/16055543.

24. Pajerowski, J. D., K. N. Dahl, F. L. Zhong, P. J. Sammak, and D. E. Discher, 2007. Physical plasticity of the nucleus in stem cell differentiation. *Proceedings of the National Academy of Sciences of the United States of America* 104:15619–15624. http://www.ncbi.nlm.nih.gov/pubmed/17893336.

25. Stephens, A. D., P. Z. Liu, E. J. Banigan, L. M. Almassalha, V. Backman, S. A. Adam, R. D. Goldman, and J. F. Marko, 2018. Chromatin histone modifications and rigidity affect nuclear morphology independent of lamins. *Mol Biol Cell* 29:220–233. https://www.ncbi.nlm.nih.gov/pubmed/29142071.

26. Davidson, P. M., C. Denais, M. C. Bakshi, and J. Lammerding, 2014. Nuclear deformability constitutes a rate-limiting step during cell migration in 3-D environments. *Cell Mol Bioeng* 7:293–306. https://www.ncbi.nlm.nih.gov/pubmed/25436017.

27. Wolf, K., M. Te Lindert, M. Krause, S. Alexander, J. Te Riet, A. L. Willis, R. M. Hoffman, C. G. Figdor, S. J. Weiss, and P. Friedl, 2013. Physical limits of cell migration: control by ECM space and nuclear deformation and tuning by proteolysis and traction force. *J Cell Biol* 201:1069–1084. https://www.ncbi.nlm.nih.gov/pubmed/23798731.

28. Norwood, L. E., T. J. Moss, N. V. Margaryan, S. L. Cook, L. Wright, E. A. Seftor, M. J. Hendrix, D. A. Kirschmann, and L. L. Wallrath, 2006. A requirement for dimerization of HP1Hsalpha in suppression of breast cancer invasion. *J Biol Chem* 281:18668–18676. http://www.ncbi.nlm.nih.gov/entrez/query.fcgi?cmd=Retrieve&db=PubMed&dopt=Citation&list_uids=16648629.

29. Kirschmann, D. A., R. A. Lininger, L. M. Gardner, E. A. Seftor, V. A. Odero, A. M. Ainsztein, W. C. Earnshaw, L. L. Wallrath, and M. J. Hendrix, 2000. Down-regulation of HP1Hsalpha expression is associated with the metastatic phenotype in breast cancer. *Cancer Res* 60:3359–3363. http://www.ncbi.nlm.nih.gov/entrez/query.fcgi?cmd=Retrieve&db=PubMed&dopt=Citation&list_uids=10910038.

30. Tretiakova, M. S., S. D. Bond, D. Wheeler, A. Contreras, M. Kocherginsky, T. G. Kroll, and T. K. Hale, 2014. Heterochromatin protein 1 expression is reduced in human thyroid malignancy. *Laboratory investigation; a journal of technical methods and pathology* 94:788–795. http://www.ncbi.nlm.nih.gov/pubmed/24840329.

31. Contreras, A., M. C. Gutierrez, and T. K. Hale, 2010. Differential Expression Patterns of the Heterochromatin Proteins HP1 alpha and HP1 beta in Different Tumor Types. *Modern Pathology* 23:385A–385A.

32. Verstraeten, V. L., and J. Lammerding, 2008. Experimental techniques for study of chromatin mechanics in intact nuclei and living cells. *Chromosome Research* .

33. Vaziri, A., H. Lee, and M. R. Kaazempur Mofrad, 2006. Deformation of the cell nucleus under indentation: Mechanics and mechanisms. *Journal of Materials Research* .

34. Li, Q., and C. T. Lim, 2010. Structure–Mechanical Property Changes in Nucleus arising from Breast Cancer.

35. Deguchi, S., K. Maeda, T. Ohashi, and M. Sato, 2005. Flow-induced hardening of endothelial nucleus as an intracellular stress-bearing organelle. *Journal of Biomechanics* .

36. Guilak, F., J. R. Tedrow, and R. Burgkart, 2000. Viscoelastic properties of the cell nucleus. *Biochemical and Biophysical Research Communications* .

37. Rowat, A. C., L. J. Foster, M. M. Nielsen, M. Weiss, and J. H. Ipsen, 2005. Characterization of the elastic properties of the nuclear envelope. *Journal of the Royal Society Interface* .

38. Rasband, W., 2014. ImageJ, U.S. National Institutes of Health, Bethesda, Maryland, USA.

39. Kapoor, P., B. D. Lavoie, and L. Frappier, 2005. EBP2 plays a key role in Epstein-Barr virus mitotic segregation and is regulated by aurora family kinases. *Mol Cell Biol* 25:4934–4945. https://www.ncbi.nlm.nih.gov/pubmed/15923612.

40. Bonilla, M. R., J. R. Stokes, M. J. Gidley, and G. E. Yakubov, 2015. Interpreting atomic force microscopy nanoindentation of hierarchical biological materials using multi-regime analysis. *Soft Matter* .

41. Yakubov, G. E., M. R. Bonilla, H. Chen, M. S. Doblin, A. Bacic, M. J. Gidley, and J. R. Stokes, 2016. Mapping nano-scale mechanical heterogeneity of primary plant cell walls. *Journal of Experimental Botany* .

42. Vinogradova, O. I., H. J. Butt, G. E. Yakubov, and F. Feuillebois, 2001. Dynamic effects on force measurements. I. Viscous drag on the atomic force microscope cantilever. *Review of Scientific Instruments* .

43. Higgins, M. J., R. Proksch, J. E. Sader, M. Polcik, S. Mc Endoo, J. P. Cleveland, and S. P. Jarvis, 2006. Noninvasive determination of optical lever sensitivity in atomic force microscopy. *Review of Scientific Instruments* .

44. Hertz, H., 1882. Ueber die Berührung fester elastischer Körper. *Journal fur die Reine und Angewandte Mathematik* .

45. Nawaz, S., P. Sánchez, K. Bodensiek, S. Li, M. Simons, and I. A. Schaap, 2012. Cell Visco-Elasticity Measured with AFM and Optical Trapping at Sub-Micrometer Deformations. *PLoS ONE* .

46. Yousafzai, M. S., F. Ndoye, G. Coceano, J. Niemela, S. Bonin, G. Scoles, and D. Cojoc, 2016. Substrate-dependent cell elasticity measured by optical tweezers indentation. *Optics and Lasers in Engineering* .

47. Guz, N., M. Dokukin, V. Kalaparthi, and I. Sokolov, 2014. If Cell Mechanics Can Be Described by Elastic Modulus: Study of Different Models and Probes Used in Indentation Experiments. *Biophysical Journal* .

48. Raudsepp, A., M. A. Williams, and S. B. Hall, 2016. Multidimensional mapping of the restoring force of an optical trap using triangular wave flow. *Journal of Modern Optics* .

49. Bacabac, R. G., D. Mizuno, C. F. Schmidt, F. C. MacKintosh, J. J. Van Loon, J. Klein-Nulend, and T. H. Smit, 2008. Round versus flat: Bone cell morphology, elasticity, and mechanosensing. *Journal of Biomechanics* .

50. Gangotra, A., and G. R. Willmott, 2019. Mechanical properties of bovine erythrocytes derived from ion current measurements using micropipettes. *Bioelectrochemistry* 128:204–210.

51. Gangotra, A., M. Biviano, R. R. Dagastine, J. D. Berry, and G. R. Willmott, 2019. Use of microaspiration to study the mechanical properties of polymer gel microparticles. *Soft matter* 15:7286–7294.

52. Hansma, P., B. Drake, O. Marti, S. Gould, and C. Prater, 1989. The scanning ion-conductance microscope. *Science* 243:641–643.

53. Hochmuth, R. M., 2000. Micropipette aspiration of living cells. *Journal of biomechanics* 33:15–22.

54. Guevorkian, K., M.-J. Colbert, M. Durth, S. Dufour, and F. Brochard-Wyart, 2010. Aspiration of biological viscoelastic drops. *Physical Review Letters* 104:218101.

55. Moreno-Flores, S., R. Benitez, M. dM Vivanco, and J. L. Toca-Herrera, 2010. Stress relaxation microscopy: Imaging local stress in cells. *Journal of biomechanics* 43:349–354.

56. Peterman, E. J., F. Gittes, and C. F. Schmidt, 2003. Laser-induced heating in optical traps. *Biophysical Journal* .

57. Kind, J., L. Pagie, H. Ortabozkoyun, S. Boyle, S. S. De Vries, H. Janssen, M. Amendola, L. D. Nolen, W. A. Bickmore, and B. Van Steensel, 2013. Single-cell dynamics of genome-nuclear lamina interactions. *Cell* .

58. Güttinger, S., E. Laurell, and U. Kutay, 2009. Orchestrating nuclear envelope disassembly and reassembly during mitosis.

59. Wandke, C., and U. Kutay, 2013. Enclosing chromatin: Reassembly of the nucleus after open mitosis.

60. Wu, P. H., D. R. B. Aroush, A. Asnacios, W. C. Chen, M. E. Dokukin, B. L. Doss, P. Durand-Smet, A. Ekpenyong, J. Guck, N. V. Guz, P. A. Janmey, J. S. Lee, N. M. Moore, A. Ott, Y. C. Poh, R. Ros, M. Sander, I. Sokolov, J. R. Staunton, N. Wang, G. Whyte, and D. Wirtz, 0. A comparison of methods to assess cell mechanical properties. *Nature Methods* .